Flying Spiders: Simulating and Modeling the Dynamics of Ballooning

Longhua Zhao, Iordanka N. Panayotova, Angela Chuang, Kimberly S. Sheldon, Lydia Bourouiba, and Laura A. Miller

Abstract Spiders use a type of aerial dispersal called "ballooning" to move from one location to another. In order to balloon, a spider releases a silk dragline from its spinnerets and when the movement of air relative to the dragline generates enough force, the spider takes flight. We have developed and implemented a model for spider ballooning to identify the crucial physical phenomena driving this unique mode of dispersal. Mathematically, the model is described as a fully coupled fluid–structure interaction problem of a flexible dragline moving through a viscous, incompressible fluid. The immersed boundary method has been used to solve this complex multi-scale problem. Specifically, we used an adaptive and distributed-memory parallel implementation of immersed boundary method (IBAMR). Based on the nondimensional numbers characterizing the surrounding flow, we represent the spider as a point mass attached to a massless, flexible dragline. In this paper, we explored three critical stages for ballooning, takeoff, flight, and settling in two

The original version of this chapter was revised. An erratum to this chapter can be found at https://doi.org/10.1007/978-3-319-60304-9_13

L. Zhao (✉)
Department of Mathematics, Applied Mathematics and Statistics, Case Western Reserve University, 10900 Euclid Avenue, Cleveland, OH 44106, USA
e-mail: longhua.zhao@case.edu

I.N. Panayotova
Department of Mathematics, Christopher Newport University, Newport News, VA 23606, USA
e-mail: iordanka.panayotova@cnu.edu

A. Chuang • K.S. Sheldon
Department of Ecology and Evolutionary Biology, University of Tennessee, Knoxville, TN 37996, USA
e-mail: angelachuang@utk.edu; ksheldon@utk.edu

L. Bourouiba
The Fluid Dynamics of Disease Transmission Laboratory, Massachusetts Institute of Technology, Cambridge, MA 02130, USA
e-mail: lbouro@mit.edu

L.A. Miller
Departments of Mathematics and Biology, University of North Carolina, Chapel Hill, NC 27599, USA
e-mail: lam9@email.unc.edu

A.T. Layton, L.A. Miller (eds.), *Women in Mathematical Biology*, Association for Women in Mathematics Series 8, DOI 10.1007/978-3-319-60304-9_10

dimensions. To explore flight and settling, we numerically simulate the spider in free fall in a quiescent flow. To model takeoff, we initially tether the spider-dragline system and then release it in two types of flows. Based on our simulations, we can conclude that the dynamics of ballooning is significantly influenced by the spider mass and the length of the dragline. Dragline properties such as the bending modulus also play important roles. While the spider-dragline is in flight, the instability of the atmosphere allows the spider to remain airborne for long periods of time. In other words, large dispersal distances are possible with appropriate wind conditions.

1 Introduction

Dispersal is the nonreturning movement of organisms away from their birth sites [25], often triggered by density and habitat-dependent factors [5, 9]. These factors play a role in the initiation and frequency of activities such as foraging, choosing nest sites, searching for mates, and avoiding predation, competition, and inbreeding [6]. Dispersal traits and mechanisms are thus wide and varied across taxa, even for organisms that disperse passively through air or water currents [19].

Spiders (Arachnida: Araneae) represent one taxon that undergoes a specialized form of passive dispersal. Besides walking from site to site, most spiders also engage in a type of aerial dispersal known as ballooning [2]. This begins with a distinctive "tiptoe" behavior where an individual straightens its legs, balancing on the tips of its tarsi. After tiptoeing, the spider raises its abdomen, releasing a silken dragline in the air (Fig. 1). Wind then allows for drag-induced lift of the whole body. Once airborne, individuals have little control over the direction and distance of displacement; rather, they join other floating life forms collectively known as "aerial plankton" [10], which are subject to air currents.

Spiders have long been observed to balloon to distances as far as 3200 km [12] and heights of up to 5 km [10]. The extreme heights and distances achieved from a seemingly simple mechanism have generated interest in the flight physics of these arachnid aeronauts. This intriguing behavior is apparently constrained by body mass ($<$100 mg) and wind speed ($<$3 m/s). The complex interactions of the physical characteristics of the spider's morphology, silk dragline properties, and meteorological conditions have also motivated the identification of the dominant regimes during takeoff, flight, and settling. Since ballooning spiders are very small and cannot be easily tracked, conventional measures of dispersal are difficult. This has motivated theoretical work in determining the physics and resulting distributions of ballooning spiders.

Early models of spider ballooning primarily focused on the factors that are important for flight as well as the distances that can be achieved (see [27] for a review of previous models). Humphrey [15] developed the first simple force balance model where the physical properties of the spider and its attached dragline were simplified to a massive sphere (spider) and a massless, rigid rod (dragline). Described as a "lollipop system," this model evaluates the possible relationships

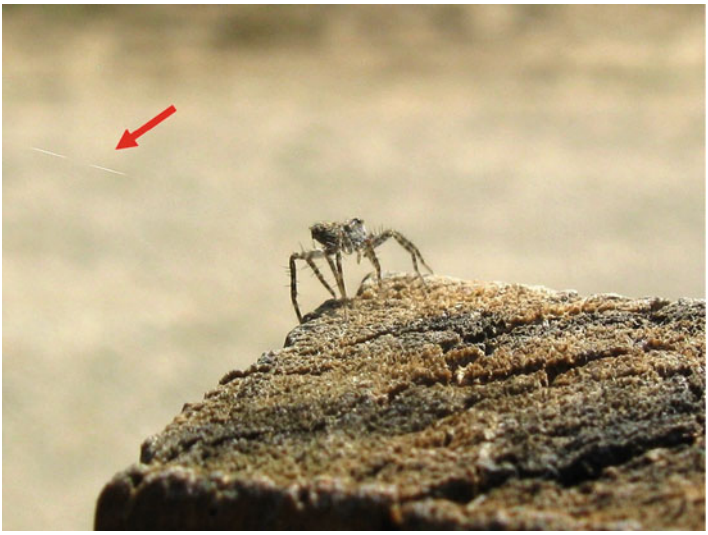

Fig. 1 Tiptoe behavior in which a spider stands on tarsi, raises the abdomen, and releases a dragline (*indicated by arrow*) in order to initiate ballooning. Photo copyright belongs to Sarah Rose

between spider mass, dragline length, and dispersal distance during initial takeoff. The results were used to define a region of physical parameters that mechanically support ballooning based on wind velocity and spider mass, although dragline length also played a role in travel speed and distance [15].

Subsequent models were built on this system by considering the dragline as a series of spheres and springs. This approach allowed more realistic properties to be included in the spider-dragline system such as flexibility and extensibility of the dragline [22]. Using a set of Lagrangian stochastic models to capture the turbulence in the air, simulations of ballooning were able to predict reasonable dispersal distances in the presence and absence of wind shear conditions [23].

Statistical approaches, empirical measurements, and simulations have also furthered our understanding of ballooning dynamics. Suter [30] measured spiders in free fall in statistical models that related the body mass and dragline lengths to their terminal velocities. The potential importance of body posturing was also noted, as it could account for deviations from the expected values of terminal velocity. In other words, spiders can possibly posture their legs and body in a way that impacts their fallout [31]. However, it is unlikely that their decision to balloon is based on accurate meteorological predictions, as shown in models that relate their probability of dispersal with mass, silk length, and local wind velocity variation. Thomas et al. used numerical simulations to understand the temporal and spatial dynamics through diffusion models [32]. These were subsequently used to understand feasible dispersal distances under a simple atmospheric model [33].

These earlier models illustrate the various methods that have been utilized to understand different aspects of the spider ballooning process but many simplifying assumptions are made regarding the fluid–structure interaction. In this study, we investigate the dominant physical regimes of passive aerial dispersal in spiders, with a particular focus on the fluid dynamics of their flight. We consider the physical parameter space that influences all stages of ballooning, including takeoff, transport, and landing. We use a numerical approach to model the complex interaction of the coupled spider-dragline system and its movement through various air-flow conditions. Like earlier studies, this model includes the spider body mass and a flexible dragline. We go beyond previous work by resolving the full aeroelasticity problem of a flexible dragline moving through a viscous fluid. We also directly simulate a variety of background air-flow profiles.

In the next section, we describe the numerical method for solving the fully coupled fluid–structure interaction problem of a flexible dragline immersed in a viscous fluid. In Sect. 2.2, we discuss our model of the spider–flow interaction and then consider the validity of our model in various scenarios: free fall in quiescent flow and nonquiescent flows. We then discuss the dynamics of ballooning in Sect. 3 in various flow conditions. Lastly, we summarize our findings in Sect. 4.

2 Methods

2.1 Immersed Boundary Method

Our goal is to mathematically model a flexible dragline that is both deformed by the air and also moves the air. In other words, we wish to consider the fully coupled fluid–structure interaction. We used the immersed boundary method to model this fully coupled fluid–structure interaction problem [18, 20, 21]. After over 30 years of application to problems in biological fluid dynamics, the immersed boundary (IB) method represents a relatively straightforward and standard approach for studying problems in animal locomotion including insect flight [17], lamprey swimming [34], and jellyfish swimming [14].

The basic idea behind the immersed boundary method is that the equations of fluid motion are solved on a (typically Cartesian) grid using an Eulerian frame of reference. The equations describing the immersed elastic boundary are solved on a curvilinear mesh defined using a Lagrangian frame of reference. The collection of Lagrangian nodes on which the equations describing the immersed elastic boundary are solved move independently of the fluid grid. The immersed boundary is moved at the local fluid velocity, and the elastic forces are spread to the fluid through regularized discrete delta functions.

The following equations describing the immersed boundary method are given in two dimensions, but the extension to three dimensions is mathematically straightforward, though efficient implementation in three dimensions is challenging. More

details may be found in Peskin [21]. The Navier–Stokes equations are used to describe a viscous incompressible fluid (such as air at low *Re*) as follows:

$$\rho(\mathbf{u}_t(\mathbf{x},t) + \mathbf{u}(\mathbf{x},t)\cdot\nabla\mathbf{u}(\mathbf{x},t)) = \nabla p(\mathbf{x},t) + \mu\nabla^2\mathbf{u}(\mathbf{x},t) + \mathbf{F}(\mathbf{x},t), \tag{1}$$

$$\nabla\cdot\mathbf{u}(\mathbf{x},t) = 0, \tag{2}$$

where $\mathbf{u}(\mathbf{x},t)$ is the fluid velocity, $p(\mathbf{x},t)$ is the pressure, $\mathbf{F}(\mathbf{x},t)$ is the force per unit area applied to the fluid by the immersed boundary, ρ is the density of the fluid, and μ is the dynamic viscosity of the fluid. The independent variables are the time t and the position $\mathbf{x}$.

The interaction equations between the fluid and the boundary are given by the following integral transforms with delta function kernels:

$$\mathbf{F}(\mathbf{x},t) = \int \mathbf{f}(r,t)\delta\left(\mathbf{x} - \mathbf{X}(r,t)\right) dr, \tag{3}$$

$$\mathbf{X}_t(r,t) = \mathbf{U}(\mathbf{X}(r,t)) = \int \mathbf{u}(\mathbf{x},t)\delta\left(\mathbf{x} - \mathbf{X}(r,t)\right) d\mathbf{x}, \tag{4}$$

where $\mathbf{f}(r,t)$ is the force per unit length applied by the boundary to the fluid as a function of Lagrangian position and time, $\delta(\mathbf{x})$ is a delta function, $\mathbf{X}(r,t)$ gives the Cartesian coordinates at time t of the material point labeled by the Lagrangian parameter r. Equation (3) applies force from the boundary to the fluid grid, and Eq. (4) evaluates the local fluid velocity at the boundary.

In order to tether the boundary points to a fixed location, a penalty force is applied that is proportional to the distance between the boundary and the desired location of target points. This force is given by:

$$\mathbf{f}(r,t) = \kappa_{targ}\left(\mathbf{Y}(r,t) - \mathbf{X}(r,t)\right), \tag{5}$$

where $\mathbf{f}(r,t)$ is the force per unit length, κ_{targ} is a stiffness coefficient, and $\mathbf{Y}(r,t)$ is the prescribed position of the target boundary. The deviations from the target position can be controlled by the parameter κ_{targ}.

The flexible dragline used in the following simulations resists stretching and bending. To model the resistance to stretching, we insert elastic links connecting adjacent boundary points that act as linear springs. Let boundary points m and n have the corresponding position coordinates $\mathbf{X}_m$ and $\mathbf{X}_n$, and let these points be connected by elastic link w. The stretching energy function for this link is then given by:

$$E_S(\mathbf{X}_m,\mathbf{X}_n) = \frac{1}{2}\kappa_s(||\mathbf{X}_m - \mathbf{X}_n|| - l_w)^2, \tag{6}$$

where l_w is the resting length of the spring and κ_s is its stiffness coefficient. Note that E_S is equal to zero when the distance between the points equals the resting length.

The dragline also has a small resistance to bending. We assume zero preferred curvature (the dragline wants to be straight). The bending energy is then given by:

$$E_b = \frac{1}{2}\kappa_b\int\left|\frac{\partial\mathbf{X}(s,t)}{\partial s}\right|^2 ds, \tag{7}$$

where κ_b is the bending stiffness. We discretize the bending energy with zero preferred curvature as follows:

$$E_b = \frac{1}{2}\kappa_b \sum_i |D_s D_s \mathbf{X}|^2 \Delta s = \frac{1}{2}\kappa_b \sum_{i=2}^{N-1} \frac{|\mathbf{X}_{i+1} - 2\mathbf{X}_i + \mathbf{X}_{i-1}|^2}{\Delta s^2} \Delta s, \tag{8}$$

The total elastic energy is calculated as the sum of the stretching and bending energies for each immersed boundary point. For example, a dragline is made up of a string of N immersed boundary points arranged in the order so that each pair of consecutive points is joined by a linear spring that resists stretching and each consecutive triplet resists bending. This results in the following equation for the total elastic energy:

$$E(\mathbf{X}_1, \mathbf{X}_2, \ldots \mathbf{X}_N, t) = \sum_{i=1}^{N-1} E_S(\mathbf{X}_i, \mathbf{X}_{i+1}) + \sum_{i=2}^{N-1} E_B(\mathbf{X}_{i-1}, \mathbf{X}_i, \mathbf{X}_{i+1}). \tag{9}$$

The elastic force at point m is then calculated using the derivatives of the elastic energy as follows:

$$\mathbf{F}_m(\mathbf{X}_1, \mathbf{X}_2, \ldots \mathbf{X}_N, t) = -\frac{\partial \mathbf{E}(\mathbf{X}_1, \mathbf{X}_2, \ldots \mathbf{X}_N, t)}{\partial \mathbf{X}_m}. \tag{10}$$

Values of the constants κ_s and κ_b must be chosen to specify reasonable energies and forces associated with the dragline and are selected to be within the range of what is observed for spiders. Mass was added to the spider using the penalty immersed boundary method [16]. The boundary points that are assigned a mass are anchored with linear springs to "ghost" massive particles. The linear springs have zero resting lengths, and the spring stiffness coefficients are chosen such that the boundary point moves with the massive particle within some tolerance. The massive particles do not interact with the fluid (the boundary points that they are connected to do) and simply move according to Newton's laws. With a stiffness spring connecting the mass point and the boundary point, an energetic penalty is imposed when the position of the Lagrangian immersed boundary point deviates from that of the mass. Similar to Eq. (5), the energetic penalty is introduced into the system by a large value of the penalty stiffness κ_s between the point of spider and the point of dragline it is attached to.

To perform direct numerical simulations, we used an adaptive and parallelized version of the immersed boundary method, IBAMR [13]. IBAMR is a C++ framework that provides discretization and solver infrastructure for PDEs on block-structured locally refined Eulerian grids [3, 4] and on Lagrangian (structural) meshes, as well as infrastructure for coupling Eulerian and Lagrangian representations. The adaptive method used four grid levels to discretize the Eulerian equations with a refinement ratio of four between levels. Regions of fluid that contained the immersed boundary or vorticity magnitude above $0.125\,\mathrm{s}^{-1}$ were discretized at the highest refinement. The effective resolution of the finest level of the grid corresponded to that of a uniform 512^2 discretization.

2.2 Spider Model

In previous mechanical models [15, 22], the spider body was modeled as a sphere (see [27] for a review of previous models). However, the detailed aerodynamics of the viscous fluid interacting with the spider-dragline system were not resolved. Based on an analysis of the relevant dimensionless numbers, which are outlined below in Sect. 2.2.2, we neglect the drag acting on the spider itself and focus on the dragline. We do consider the mass of the spider which is represented as a point mass tethered to the dragline. The dragline is modeled as a massless beam that resists bending and stretching. The governing equations are similar to Eqs. (1)–(2) as following:

$$\rho(\mathbf{u}_t(\mathbf{x},t) + \mathbf{u}(\mathbf{x},t)\cdot\nabla\mathbf{u}(\mathbf{x},t)) = \nabla p(\mathbf{x},t) + \mu\nabla^2\mathbf{u}(\mathbf{x},t) + mg + \mathbf{F}(\mathbf{x},t), \quad (11)$$

$$\nabla\cdot\mathbf{u}(\mathbf{x},t) = 0, \quad (12)$$

where mg is the gravity force due to the point mass of the spider and $\mathbf{F}$ is the force that the dragline applies to the fluid.

For the numerical discretization of the elastic dragline, the dragline is represented as discrete Lagrangian points connected by springs that resist bending and stretching with stiffnesses κ_s and κ_b, respectively. Note that the relevant elasticity Eqs. (5)–(7) represent a very different system from the chain of springs in Reynolds et al.'s model [22]. In Reynolds et al.'s model, the dragline is defined by spring modulus K only, i.e., κ_s in our model. Their dragline can freely bend in any direction, which may result in unrealistic entanglement. In our model, the bending modulus limits the bending of the dragline. Our model may still, however, result in some entanglements due to the fluid–structure interaction. Note that we do not include electrostatic forces in our model which may further limit the degree of entanglement.

The spider-dragline system is then immersed in air with appropriate boundary conditions for different scenarios (e.g., no slip for settling in a quiescent fluid, Dirichlet for prescribed background flow, and mixed for cavity flow). In this fluid–structure interaction system, the flow field is obtained by numerically solving the full Navier–Stokes Eqs. (11)–(12). The spider-dragline is moved at the local fluid velocity (4).

2.2.1 Numerical and Physical Parameters Used for Simulation

Due to the computational challenges associated with immersed boundary simulations in three dimensions, we consider only a two-dimensional representation of the spider-dragline system in this initial study. Note that in two dimensions, the spider is actually a sheet, and the point mass representing the spider is with units of mass per length (M/L) converted from the three-dimensional mass. As a rough approximation of the relationship between the actual mass of a real spider and the two-dimensional idealization, one could divide the mass of a spider by its diameter to obtain the mass per unit length used in the simulations.

Parameters used for the simulation are summarized in Table 1.

Table 1 Parameters used in the numerical simulations

Physical parameters	Values in literature	Values in simulation
Elasticity (Spring modulus)	n/a	20 (N/m)
Bending modulus	n/a	$10^{-5} \sim 5 \times 10^{-4}$ (N·m)
Dragline length [2, 22]	$0 \sim 2.3$ (m)	$0.05 \sim 0.2$ (m)
Dragline diameter [26]	20–100 (nm)	Line
Dragline density [29]	$1.1 \sim 1.4$ g/cm^3	Massless
Spider diameter [8, 24]	$1 \sim 5$ (mm)	Pointwise
Spider mass [8, 30]	$0.09 \sim 84.70$ (mg)	$2 \sim 800$ (mg/m)
Air mass density [1]	1.165 (kg/m^3)	1.177 (kg/m^3)
Air dynamic viscosity [1]	1.86×10^{-5} (N·s/m^2)	1.846×10^{-5} (N·s/m^2)

Note the difference in the units of stiffness and mass since the simulations are in two dimensions rather than three dimensions for actual spiders. The physical properties of the air are at temperature 30 °C [1]

2.2.2 Dimensionless Parameters

Dimensionless parameters are important to characterize the properties of the fluid and its interaction with the organism. The first dimensionless parameter we consider is the Reynolds number (Re), which is computed as the ratio of inertial forces over viscous forces. Re is given as $\frac{\rho LU}{\mu}$, where ρ is the density of the fluid, μ is the dynamic viscosity of the fluid, L is a characteristic length that is chosen based on the application, and U is a characteristic velocity. Re is often used to characterize different flow regimes. When Re is low ($Re << 10^3$), the flow is in the laminar regime. When $Re << 1$, viscous forces are dominant, the flow is reversible, and the fluid motion is smooth. For $Re >> 1$, the flow is dominated by inertial forces. Flows at $Re > 2300$ (for the case of pipe flow) are typically, but not necessarily, turbulent and tend to produce chaotic eddies, vortices, and other flow instabilities.

There are several ways that one can choose the characteristic length for the calculation of Re. In Humphrey's model [15], the Reynolds number is defined as $Re_D = \frac{\rho D|\mathbf{V}|}{\mu}$, where D is the diameter of spider and $|\mathbf{V}|$ is the modulus of the wind velocity. In our simulations, we choose U as the velocity of the spider relative to the air. The characteristic length L could be chosen as the dragline length ℓ (Re_ℓ), the radius of the dragline d (Re_d), or the spider body diameter D (Re_D), respectively. Keeping the same characteristic velocity, Re varies with ratios from 1 to 10^4 for different choices of characteristic length L, using the radius of the dragline d and the length of dragline ℓ.

Another important dimensionless parameter is the Richardson number Ri. It is defined as the ratio of density gradient over the flow gradient. Ri is used as the threshold parameter for convective instability, which is an environment factor that may be important in the decision to balloon. Thomas et al. [33] reported that the number of airborne spiders was significantly correlated with Richardson numbers. In our study, we explore the dynamics of airborne spiders and neglect the influence of temperature. Winds are specified as the boundary and initial conditions. Besides

temperature, we also neglect the effect of electrostatics in the model. Because electrostatic forces can prevent sticking, coiling, and entanglement of the dragline, and because Gorham [11] reported that the effects of electrostatic forces could be substantial for distances traveled, we plan to include electrostatic forces in our future work.

The last dimensionless number considered is the Strouhal number (**St**), defined as:

$$\mathbf{St} = \frac{L}{U\tau}.$$

Here, τ is the relaxation characteristic time scale or the inverse of disturbance frequency f. **St** represents a measure that relates oscillation frequency to fluid velocity. For the case of spider ballooning, the oscillations in fluid velocity are due to alternate vortex shedding from the end of the dragline. Note that for $\mathbf{St} << 1$, oscillations of the fluid have a minimal impact on the dynamics. At intermediate Strouhal numbers $0.1 < \mathbf{St} < 1$, oscillation is characterized by the buildup and rapidly subsequent shedding of vortices [28]. Such vortex shedding could be important to spider ballooning since large forces are generated during vortex separation. Such peaks in force may impact takeoff and flight trajectories.

2.2.3 Boundary and Flow Conditions

The background flows are driven in the simulations using Dirichlet boundary conditions. In the quiescent fluid simulations, where we study the free fall of spiders, zero initial and boundary velocities are used. For various background flows, we specify the wind velocity on the boundary of the domain. The velocities are initially zero everywhere, and the flow velocities at the boundaries are increased until the target background velocity is reached. For the cases of cavity flow, the bottom and sides of the domain are fixed at zero velocity. The top boundary condition is continuous functions in time with zero initial value. Details about the boundary conditions are provided in Sect. 3 with the results.

3 Results

To identify the crucial physical properties for spider ballooning, we solve the fully coupled fluid–structure interaction problem using the immersed boundary method. The numerical simulations are performed with IBAMR (revision 3803) [13] for a single massive spider attached to a flexible, massless dragline. We first consider the spider-dragline system free-falling in a quiescent fluid. We then numerically simulate the free movement of the spider-dragline in uniform background flow and in cavity flow (to approximate the conditions of an eddy). To reveal the dynamics of

takeoff, we tether the spider-dragline system in both uniform and cavity flows and release it after a certain time period. In the quiescent fluid simulations, the bottom boundary of the computational domain is modeled as ground without penetration. In the simulations with uniform background flow, the boundary conditions are set to the prescribed target velocity. In the cavity flow simulations, the bottom and sides of the domain have zero velocity boundary conditions, and the top is set to a uniform velocity.

3.1 Free Fall in a Quiescent Fluid

The spider-dragline system is immersed in quiescent air. Due to gravity, the spider-dragline system free-falls and generates air flow around it. The vorticity

$$\omega = \nabla \times \mathbf{u}$$

of a two-dimensional flow is always perpendicular to the two-dimensional plane and describes the local rotating motion. Therefore, we consider it a scalar field and visualize the flow by its vorticity. Figure 2 shows four snapshots of vorticity during the free fall in a quiescent fluid. Except for the mass of the spider, all other parameters and initial and boundary conditions are set to the same values for these figures. The mass per unit length is set to $M = 2 \times 10^{-6}$, 2×10^{-5}, 4×10^{-5}, and 2×10^{-4} kg/m, respectively. The other key parameters are dragline length $\ell = 0.1$ m, beam bending stiffness constant $\kappa_b = 5.0 \times 10^{-15}$ N·m, spring stiffness coefficient $\kappa_s = 20$ N/m, and the initial position of the dragline's middle point $(x_0, y_0) = (0, 0.15)$.

As the mass of the spider increases, the spider-dragline system falls faster to the ground. The spider-dragline system falls slowly with the smallest mass ($M = 2 \times 10^{-6}$ kg/m), and the vorticity is plotted at time $t = 8$ s in Fig. 2a. For the larger masses, the vorticity is plotted before the spider-dragline system reaches the ground (Fig. 2b-c). Note that red indicates clockwise vorticity and blue indicates counterclockwise vorticity. In the case of the smallest mass, we observe smooth, streaming flow. For the larger masses, $M = 4 \times 10^{-5}$ and 2×10^{-4} kg/m, vortices are alternately shed from the end of the dragline. For the intermediate case, $M = 2 \times 10^{-5}$ kg/m, the vorticity generated by the dragline induces oscillations of the dragline. These phenomena are consistent with the Reynolds number computed using the average settling velocity as the characteristic velocity and the length of the dragline as the characteristic length. For these four simulations, the Reynolds numbers Re_ℓ are about 146, 960, 1450, and 3320, respectively.

To reveal more of the dynamics during the spider-dragline free fall in a quiescent air, Fig. 3 shows the vertical velocity dy/dt of the bottom point of the dragline (the location of the point mass) vs. time. Figure 3a compares the four simulations in which the masses per unit length are varied. For $M = 2 \times 10^{-6}$ kg/m (Fig. 3b), the system falls slowly and continues to accelerate during the entire length of

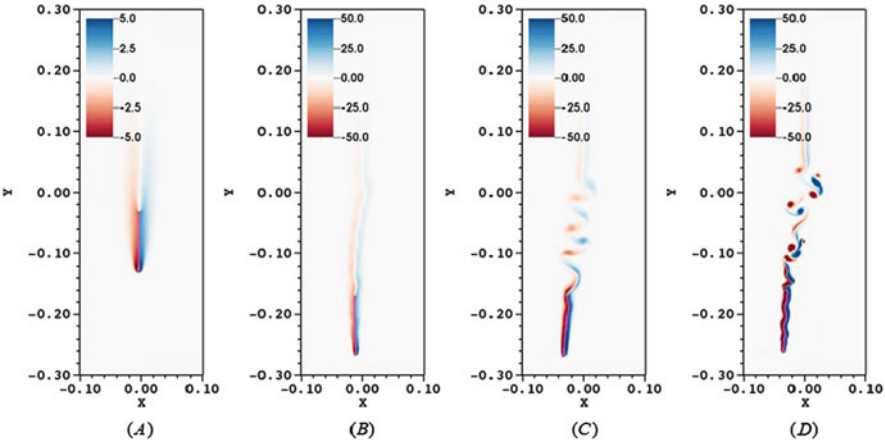

Fig. 2 Vorticity (s^{-1}) of the flow generated by the spider-dragline system during free fall in a quiescent fluid with the spider's mass per unit length set to $M = 2 \times 10^{-6}$, 2×10^{-5}, 4×10^{-5}, and 2×10^{-4} kg/m, respectively. The other parameters are held constant for this set of simulations: string length $\ell = 0.1$ m, beam bending stiffness $\kappa_b = 5 \times 10^{-15}$ N·m, spring stiffness coefficient $\kappa_s = 20$ N/m, and initial position of the middle point $(x_0, y_0) = (0, 0.15)$. Vorticity plots in this paper are generated by VisIt [7]. (**a**) $M = 2 \times 10^{-6}$ kg/m. (**b**) $M = 2 \times 10^{-5}$ kg/m. (**c**) $M = 4 \times 10^{-5}$ kg/m. (**d**) $M = 2 \times 10^{-4}$ kg/m

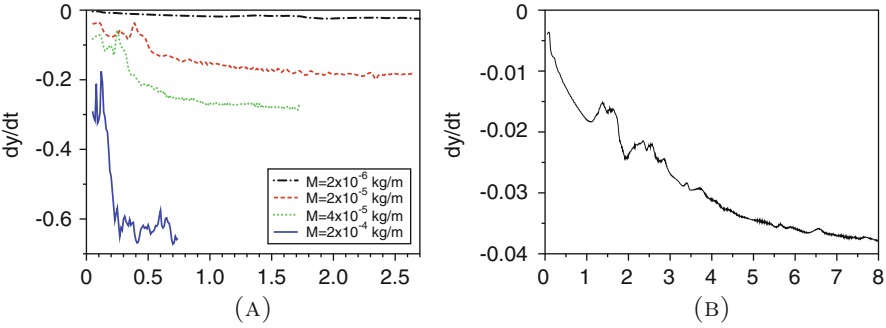

Fig. 3 Vertical velocity (m/s) of the bottom point of the dragline where the spider mass is located. Results are shown for (**a**) the comparison for spiders with masses per unit length of $M = 2 \times 10^{-6}$, 2×10^{-5}, 4×10^{-5}, and 2×10^{-4} kg/m, and (**b**) longer period for spiders with $M = 2 \times 10^{-6}$ kg/m. Except for $M = 2 \times 10^{-6}$ kg/m, the curves end when the spider-dragline reaches the ground

the simulation ($t \leq 8$ s). For the other three masses, vortices develop behind the dragline, the terminal velocities are quickly reached, and the spiders reach the ground before $t = 3$ s. After the spider approaches the ground, the vertical velocity of the dragline is almost zero, except when it waves back and forth horizontally.

Since the dragline velocity sets the effective *Re* of the system, we report the average terminal velocities (or settling speeds) for the different cases as illustrated in Figs. 4 and 5. The average settling speed is computed as the average speed of the middle of the dragline before the spider-dragline system reaches the ground.

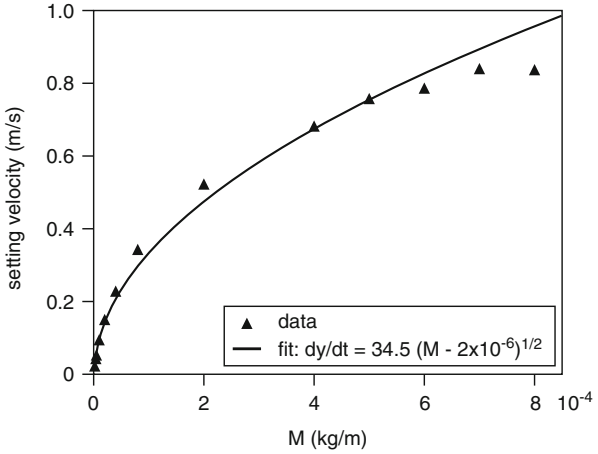

Fig. 4 The average settling velocity (m/s) vs. the spider mass per unit length (kg/m) with the masses set to $M = 2 \times 10^{-6} \sim 8 \times 10^{-4}$ kg/m. The spider-dragline system free-falls in the quiescent air with the dragline length fixed at $\ell = 0.1$ m, spring stiffness coefficient set to $\kappa_s = 20$ N/m, bending modulus fixed at $\kappa_b = 5 \times 10^{-15}$ N·m, and initial position of the middle point set to $(x_0, y_0) = (0, 0.15)$

Figure 4 shows the average settling speed for different masses per unit length with a fixed dragline length $\ell = 0.1$ m. From these results, we see that settling velocity monotonically increases as the mass of the spider increases. Figure 5 shows the average settling speed for different dragline lengths with a fixed spider mass per unit length of $M = 2 \times 10^{-4}$ kg/m. The shorter the dragline, the larger the average settling velocity of the spider-dragline. With a linear least square fit, the relation between the settling velocity vs. the dragline length is $\frac{dy}{dt} = 0.682 - 1.536\ell$. The settling velocity as a function of the spider mass is nonlinear. Using a power fit, we find that $\frac{dy}{dt} = 34.5\sqrt{m - 2 \times 10^{-6}}$.

Recall that in Humphrey's model [15], the dragline is rigid. In the study by Reynolds el al. [22, 23], the silk dragline is described as a line of springs joined at nodes. Those springs themselves are stretchable. At the nodes, the dragline can freely bend in any direction. To more accurately model the dragline, we introduced resistance to bending that is proportional to the bending stiffness modulus, κ_b, as given in Eq. (7). Figure 6 shows the horizontal drift that results from only changing the bending modulus κ_b. We observe that there is no pattern between the direction and magnitude of the horizontal shift and the bending moduli. The direction of the shift depends upon the side on which the first vortex separates from the dragline, highlighting the complicated interaction of the elastic dragline and the fluid.

For all subsequent simulations in Sects. 3.2–3.3, we keep the dragline length fixed at $\ell = 0.1$ m, the bending stiffness set to $\kappa_b = 5 \times 10^{-15}$ N·m, and the spring stiffness coefficient set to $\kappa_s = 20$ N/m. To directly compare the results between different scenarios, we set all other physical parameters to the values used in Fig. 2.

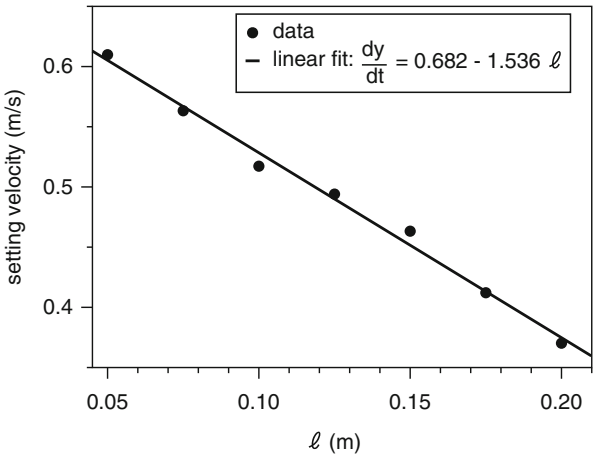

Fig. 5 The average settling velocity vs. the dragline length ℓ (m) varied from $0.075 \sim 0.2$ with the spider mass per unit length set to $M = 2 \times 10^{-4}$ kg/m. The spider-dragline free-falls in the quiescent air with other parameters fixed to the same values as shown in Fig. 4

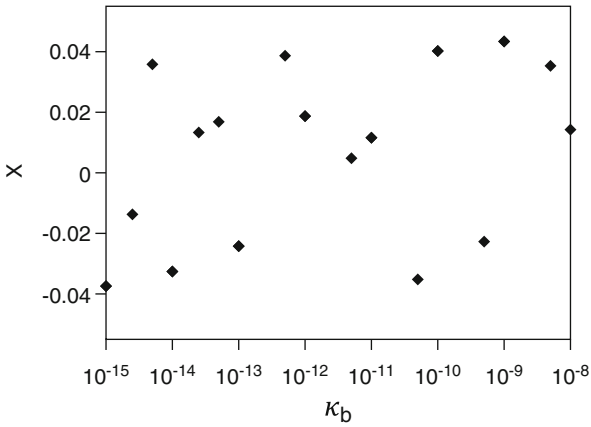

Fig. 6 Horizontal shift x (m) as a function of the beam bending stiffness modulus κ_b (N·m) when the spider-dragline free-falls in quiescent fluid. Spider mass $M = 2 \times 10^{-4}$ kg/m, dragline length $\ell = 0.1$ m, and spring stiffness coefficient $\kappa_s = 20$ N/m

3.2 Free Fall with Background Flows

As spider ballooning is greatly influenced by local meteorological conditions, we simulate spider free fall with two different types of background flows. The first is a uniform background wind and the second is a cavity flow driven by a horizontal velocity at the top of the domain. Note that cavity flow is used to approximate the behavior of a spider ballooning in an eddy. Recall from the free fall results in quiescent air, a spider with a shorter dragline falls faster. In this section, we keep the dragline fixed at $\ell = 0.1$ m. Extrapolating from the study in quiescent air, we can predict that spiders with longer draglines in background flow will also fall more slowly and stay suspended in air for longer periods of time.

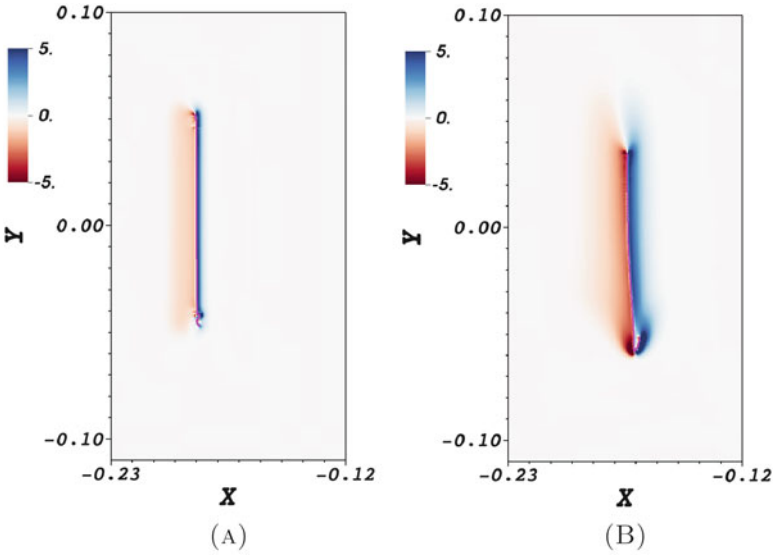

Fig. 7 Vorticity generated by the spider-dragline system free-falling in a uniform background wind with $U = V = 0.008$ m/s, where the prescribed boundary conditions are set to $\mathbf{u}(x,t) = [U,V]^T$. The mass per unit length of the spider is $M = 2\times10^{-6}$ kg/m. (**a**) t = 1.25 s. (**b**) t = 3.25 s

3.2.1 Uniform Background Flows

The vorticity fields in Fig. 7 show the case when the spider-dragline system free-falls in a 45° uniform wind with a constant velocity $[U,V] = [0.008, 0.008]^T$ m/s, where the boundary condition for the simulation was set to $\mathbf{u}(x,t) = [U,V]^T$. The mass per unit length of the spider was set to $M = 2 \times 10^{-6}$ kg/m. Compared to falling in quiescent air, these vorticity plots show slight asymmetry due to the background wind. The vortex developed on the left (upwind direction) side of the dragline has a larger area than on the left side of the dragline as Fig. 7a, but the bottom of the dragline is continually deforming as vorticity grows near the curved tip (seen Fig. 8b). For this set of parameters, the spider-dragline mostly moves with the air.

The profiles in Fig. 8 show the positions of the dragline when the spider-dragline system free-falls in the background winds, which are in the same direction (45°) but with different strengths. The time increment dt between each dragline is 0.25. The velocities of the uniform wind are $[U,V]^T = [0.01, 0.01]^T$, $[0.008, 0.008]^T$, and $[0.005, 0.005]^T$ m/s, respectively. Note that for these simulations, the spider-dragline system has a spider mass per unit length set to $M = 2\times10^{-6}$ kg/m, a dragline length fixed at $\ell = 0.1$ m, beam bending stiffness constant set to $\kappa_b = 5 \times 10^{-15}$ N·m, and spring stiffness coefficient set to $\kappa_s = 20$ N/m. The initial position of the dragline is the dotted line in the figures. With a stronger background wind, advection dominates. The spider-dragline system goes with the flow with little deformation.

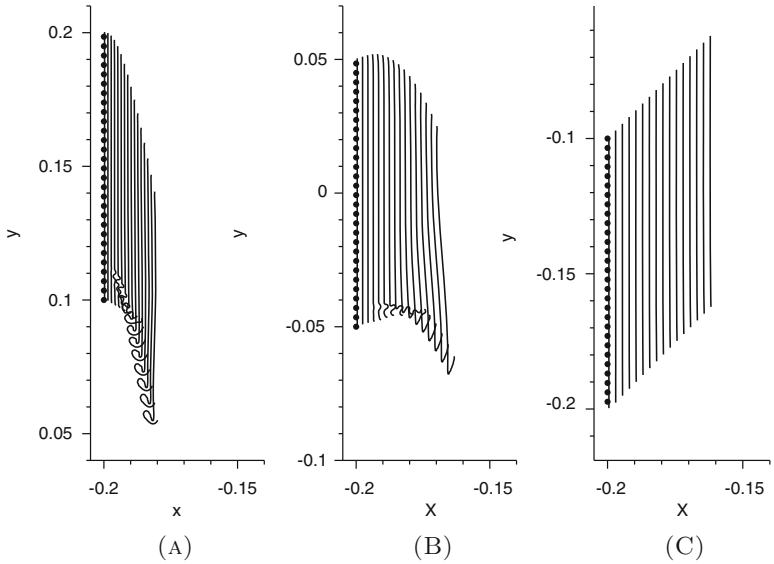

Fig. 8 Positions of the dragline at different snapshots in time with the time increment $dt = 0.25$ s between each dragline. The spider-dragline falls in the background wind (U, V) with different strengths. The *black dotted line* is the initial position. (**a**) $U = V = 0.005$ m/s, (**b**) $U = V = 0.008$ m/s, and (**c**) $U = V = 0.01$ m/s. The spider mass per unit length is set to $M = 2\times10^{-6}$ kg/m

In particular, we observe no entanglement as was reported in Reynolds et al. [22]. Compared to the wind speeds observed for tiptoeing behavior, for example, 1.7–2.6 m/s for *Pardose purbckenisis* [24], the background wind in our study is much weaker. For stronger winds, the spider-dragline system would advect out of the computational domain in a very short period with a similar profile as Fig. 8c. When the background wind is weaker, small deformations appear at the tip of the dragline where the spider is attached, likely due to shearing and the formation of vorticity. Note that the bending modulus is very small relative to the strength of the wind, and the dragline behaves as an extremely flexible line.

Changing the angle of the wind relative to the horizontal and keeping its magnitude constant, we demonstrate the sequence positions of the dragline in Fig. 9. The time increment between each dragline is the same as in Fig. 8, i.e., $dt = 0.25$ s. The spider mass per unit length is set to $M = 2 \times 10^{-6}$ kg/m, and the initial position of the middle point is fixed at $(x_0, y_0) = (-0.2, -0.15)$. The direction of the wind has a significant effect on the trajectory of the ballooning spider. The horizontal component determines the distance it travels along the landscape, and the vertical component combined with the mass of the spider determines whether the spider will land or fly up. With a vertical wind (Fig. 9d), horizontal movement is negligible. Figure 9a presents the situation in which the spider-dragline systems free-fall in a weak horizontal breeze.

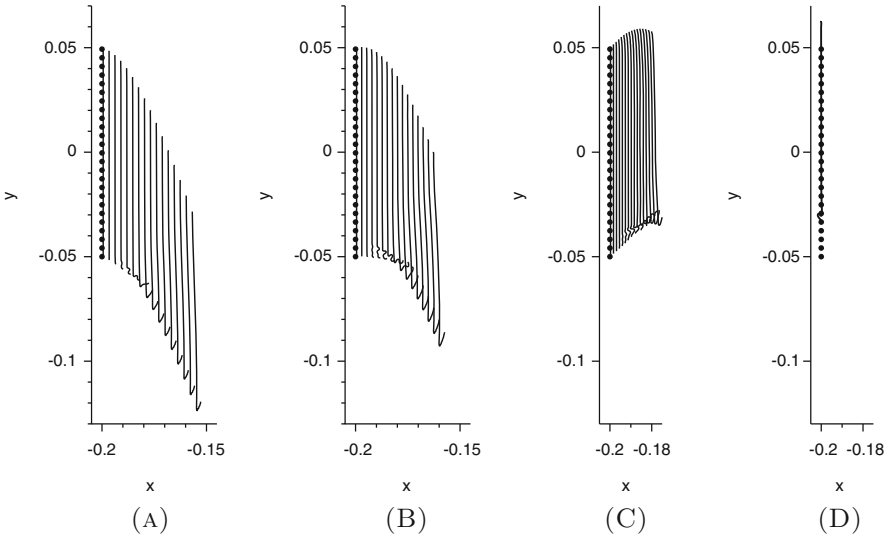

Fig. 9 Profiles of draglines in wind with fixed magnitudes of velocity but different directions: (**a**) horizontal wind, (**b**) 30°, (**c**) 60°, and (**d**) vertical wind. The *black dotted line* indicates the initial position. For the vertical wind case (**d**), only the initial and the end positions in that time period were plotted as there is almost no horizontal movement. Wind strength is fixed at $|\mathbf{U}| = 0.008\sqrt{2}$ m/s. Note that Fig. 8c shows a 45° wind of the same magnitude

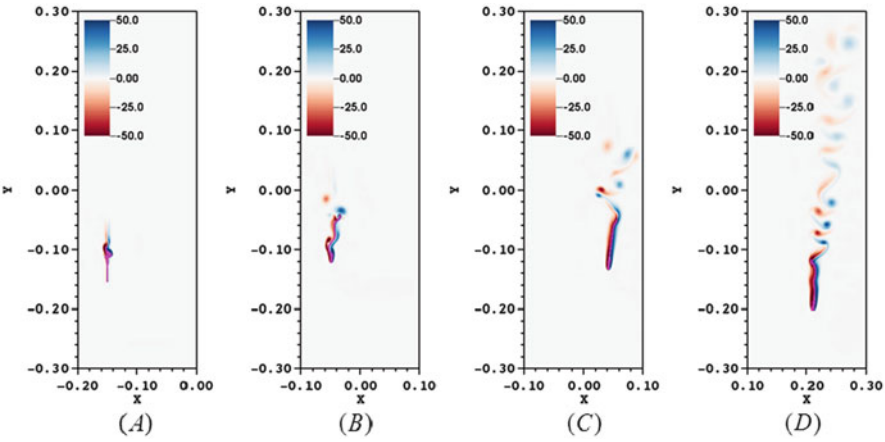

Fig. 10 Vorticity (s^{-1}) snapshots of the flow generated by the spider-dragline system with a 45° background wind, $(U, V) = (0.2, 0.2)$ m/s, at different times. The spider mass $M = 4\times10^{-5}$ kg/m. (**a**) $t = 0.25$ s. (**b**) $t = 0.75$ s. (**c**) $t = 1.25$ s. (**d**) $t = 2.25$ s

With a different spider mass $M = 4 \times 10^{-5}$ kg/m, Figs. 10 and 11 provide more details for the flow field and the dragline when the spider-dragline system free-falls in the 45° uniform wind, $(U, V) = (0.2, 0.2)$ m/s. Other parameters are matched

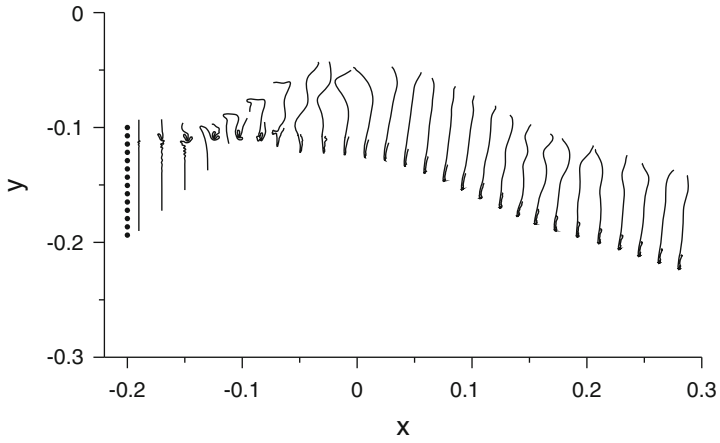

Fig. 11 Positions of the dragline at different times during the simulation. The time increment *dt* between draglines is 0.1 s. The *dotted line indicates* the initial position. The spider-dragline is flying from the left to the right with the flow. The spider mass is set to $M = 4 \times 10^{-5}$ kg/m and the uniform background wind blows 45° with respect to the horizontal and with $(U, V) = (0.2, 0.2)$ m/s

to those reported in Figs. 7, 8 and 9: the dragline length is set to $\ell = 0.1$ m, the bending stiffness is set to $\kappa_b = 5 \times 10^{-15}$ N·m, the spring stiffness is $\kappa_s = 20$ N/m, and the initial position of the middle point is given by $(x_0, y_0) = (-0.2, -0.15)$. As seen in Fig. 2c, the mass per unit length of the spider is sufficient to strongly shear the fluid, resulting in vortex shedding from the tip of the dragline. The magnitude of the resulting vorticity is stronger than for the case of a uniform background wind. Figure 11 shows the profiles of the dragline during the flight. The time increment *dt* between draglines is 0.1. The spider-dragline system moves up due to the background wind and then moves down as the effect of the gravity decelerates the system and produces negative settling velocities. Deformation of the dragline initially occurs toward the top of the dragline as vortices are shed. Eventually, the whole dragline is twisted and later the top of the dragline straightens while the bottom is curved.

In Fig. 12, the spider's mass per unit length is set to $M = 2 \times 10^{-5}$ kg/m. Two snapshots of the vorticity field are shown for free fall in a 45° background wind with $|\mathbf{U}| = 0.2$ m/s. Initially the flow relative to the dragline system is smooth, and eventually vortices develop and are shed from the tip. These vortices induce deformations in the dragline. After some time, the dragline and spider get entangled. These dynamics are distinct from the case of free fall in a quiescent fluid.

Figure 13 shows the profiles of the dragline with winds in three different directions, i.e., 30°, 45°, and 60°. The strength of the wind is fixed at $|\mathbf{U}| = 0.2$ s. The green line is the initial position for all three cases. The time increment *dt* between draglines is 0.15 s. After the spiders are advected about 0.1–0.2 m, the spider and dragline become entangled, resulting in a stable configuration. It is

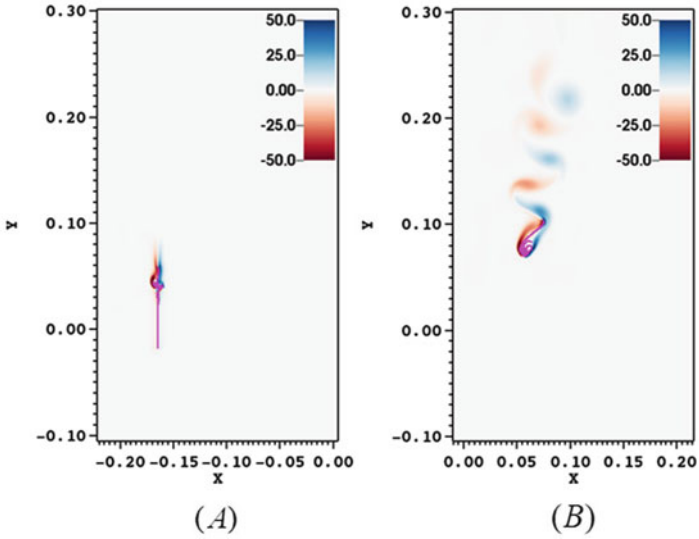

Fig. 12 Snapshots of vorticity (s^{-1}) of the flow during free fall of the spider-dragline with background wind set to $|\mathbf{U}| = 0.2$ m/s at 45° from horizontal. The spider's mass per unit length is set to $M = 2 \times 10^{-5}$ kg/m. The dragline-spider system is shown in pink. (**a**) $t = 0.25$ s. (**b**) $t = 2$ s

possible that this entanglement effectively generates a large surface area that also acts to generate sufficient drag to keep the spiders afloat. By varying the direction of the wind, we change the horizontal and vertical velocity components but keep the same strength of the wind. With a large vertical component (60° wind, blue profiles in Fig. 13), the spider-dragline system keeps rising in the air, while its horizontal shift is decreased compared with the other directions (red and black profiles). In the intermediate case (45° shown in red), the spider-dragline system advects beyond the computational domain. With the smallest vertical component (30° in Fig. 13), the spider-dragline system descends and will drop to the ground eventually, unless the wind direction or speed is changed.

Figure 14 shows the vertical velocity profile for the dragline's tip, where the spider is attached, when the spider-dragline free-falls in uniform winds of the same strength ($|\mathbf{U}| = 0.2$ m/s) but different directions. The spider mass per unit length was fixed at $M = 2 \times 10^{-5}$ kg/m. Initially, the spider moves with the background flow. Due to gravity, the spider-dragline system begins to decelerate. The movement of the spider against the background flow causes shearing, vortex formation, and eventual oscillations in the vertical velocity. The black curve for the 30° wind ends earlier than the other two curves since the spider-dragline system has left the $[-0.3,\ 0.3] \times [-0.3, 0.3]$ computational domain.

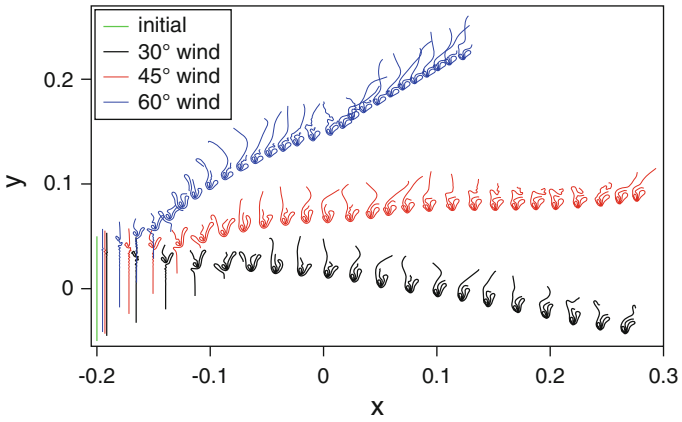

Fig. 13 Profiles of draglines in wind of the same magnitude, $|\mathbf{U}| = 0.2$ m/s, but different directions from the horizontal, 30°, 45°, and 60°, respectively. The *green line* is the initial position. *Blue* is used for 60° wind, *red* for 45° wind, and *black* for 30° wind. The time increment dt between draglines is 0.15 s. The spider's mass per unit length is $M = 2 \times 10^{-5}$ kg/m, and the initial position of the middle point is $(x_0, y_0) = (-0.2, 0)$

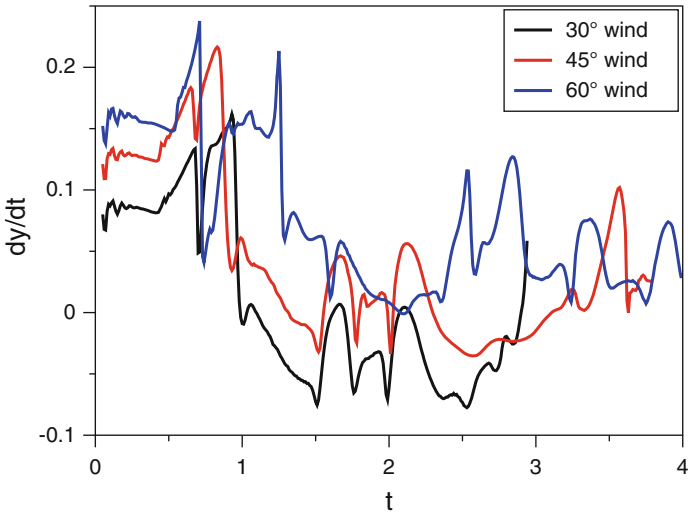

Fig. 14 Vertical velocity vs. time of the spider-dragline system in winds of the same magnitude ($|\mathbf{U}| = 0.2$ m/s) but from different directions

3.2.2 Free Fall in a Cavity Flow

In Sect. 3.2.1, we considered spider ballooning with a uniform background wind. The relevant meteorological conditions for ballooning are not, however, always as simple as uniform flow. To explore the spider ballooning in nonuniform flow, we

simulate the spider-dragline system free fall in a "lid-driven" square cavity flow. Such flows roughly approximate the conditions of ballooning with an eddy.

The no-slip velocity boundary condition ($U = V = 0$) was applied on the bottom and sides of the domain. On the top of the domain, the velocity was set to $U \neq 0$ and $V = 0$. This models a moving lid in a box, which forms an eddy. To avoid the discontinuity for the initial condition, we set the velocity at the top boundary of the domain to a hyperbolic tangent function given by $U = 3\tanh(100t)$ m/s. With this boundary condition, results for the two different spider masses per unit length are considered, $M = 2 \times 10^{-5}$ kg/m and 4×10^{-5} kg/m.

Figure 15 shows vorticity snapshots of the spider-dragline system in a cavity flow. The time values for these vorticity plots are t = 0.6, 0.65, 1, 1.5, 2.2, 2.5, 3, 3.5, and 4 s, respectively. The flow velocity in the domain is initially set to zero. The

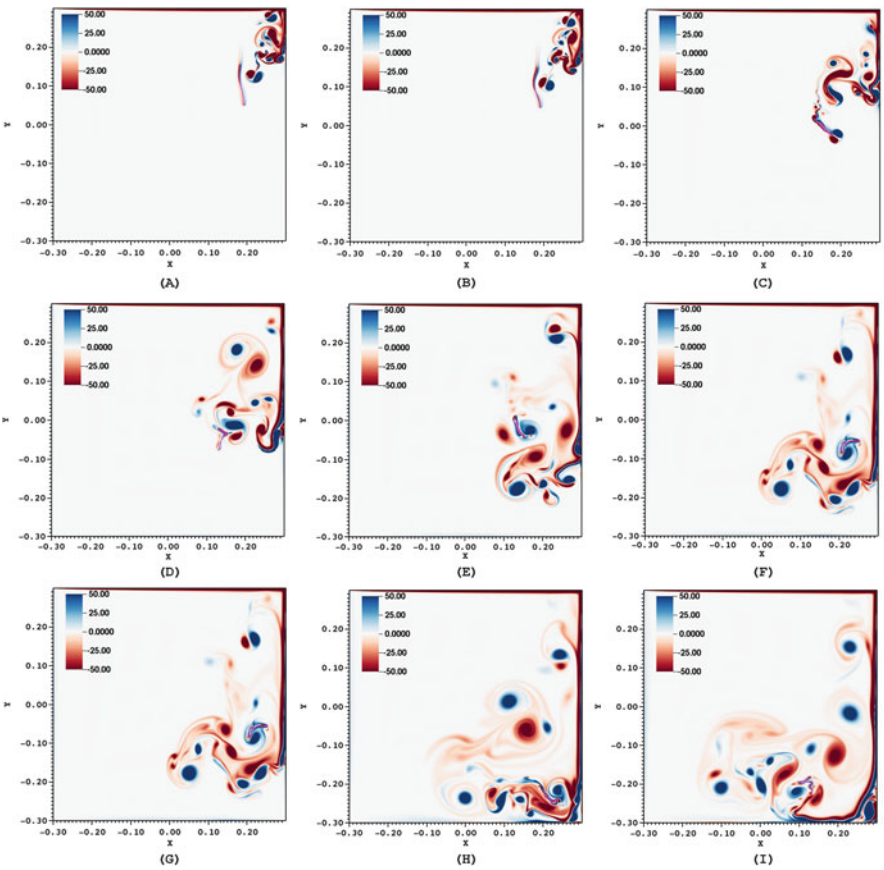

Fig. 15 Vorticity (s^{-1}) snapshots of the spider-dragline system in a cavity flow with background velocity $U = 3\tanh(100t)$ m/s at the top of the domain and the spider mass per unit length is set to $M = 2 \times 10^{-5}$ kg/m. (**a**) t = 0.6 s. (**b**) t = 0.65 s. (**c**) t = 1 s. (**d**) t = 1.5 s. (**e**) t = 2.2 s. (**f**) t = 2.5 s. (**g**) t = 3 s. (**h**) t = 3.5 s. (**i**) t = 4 s

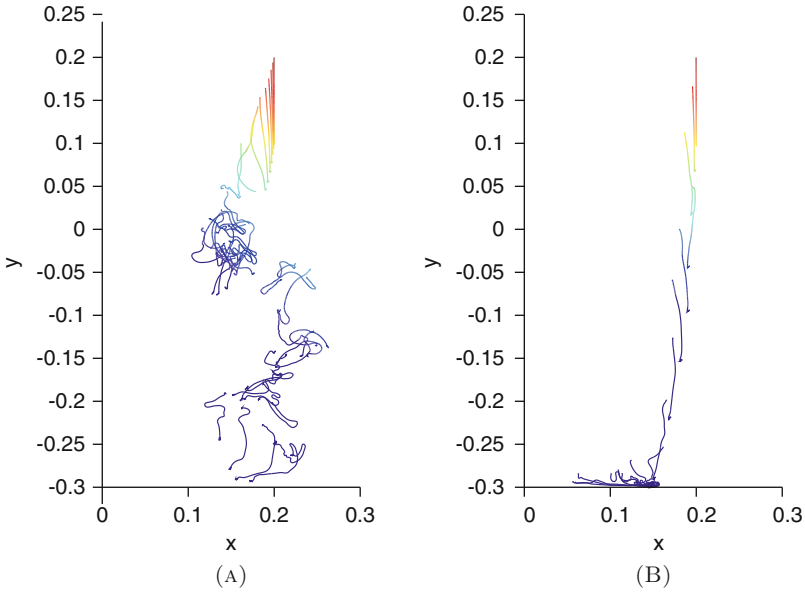

Fig. 16 Dragline vs. time in the cavity flow $U = 3\tanh(100t)$ m/s. The colormap is of the dragline changes from red to blue during the time. (**a**) The spider mass per unit length is $M = 2\times10^{-5}$ kg/m and the time increment dt between draglines is 0.1 s; (**b**) the spider mass per unit length is $M = 4 \times 10^{-5}$ kg/m and the time increment dt is 0.25 s

spider begins to fall as the flow develops. Notice that vortices develop in the upper right corner of the domain due to the velocity at the top. As the cavity flow develops, the spider-dragline system interacts with these vortices in complicated ways.

Figure 16 shows temporal snapshots of the dragline for spiders with masses per unit length of $M = 2 \times 10^{-5}$ kg/m and $M = 4 \times 10^{-5}$ kg/m. The initial positions are the same for both simulations. The time increment dt between draglines is 0.1 s for Fig. 16a; while $dt = 0.25$ s for Fig. 16b. More frames are plotted to show the dynamics in Fig. 16a. The lighter spider, Fig. 16a, settles slowly and eventually interacts with the vortices developed in the cavity flow. During this interaction, the spider-dragline system becomes entangled. For the heavier spider with mass per length set to $M = 4 \times 10^{-5}$ kg/m, the situation is simple: The spider settles before the cavity flow develops. Note that more frames are shown in the plot for $M = 2 \times 10^{-5}$ kg/m than for $M = 4 \times 10^{-5}$ kg/m in Fig. 16b since the snapshots end when the spider hits the ground.

Figure 17 shows the vertical velocity of the bottom point of the dragline vs. time, which corresponds to the dragline profiles shown in Fig. 16. The heavy spider with $M = 4\times10^{-5}$ kg/m, shown as the blue curve, has a large downward vertical velocity until it hits the ground around $t = 2$ s. Recall that it falls to the ground before the cavity flow develops, and no upward motion is observed. For the lighter spider with mass per unit length set to $M = 2 \times 10^{-5}$ kg/m, the vertical velocity oscillates from positive to negative. Positive velocity can be attributed to the interaction of the spider-dragline with the background vortices due to cavity flow.

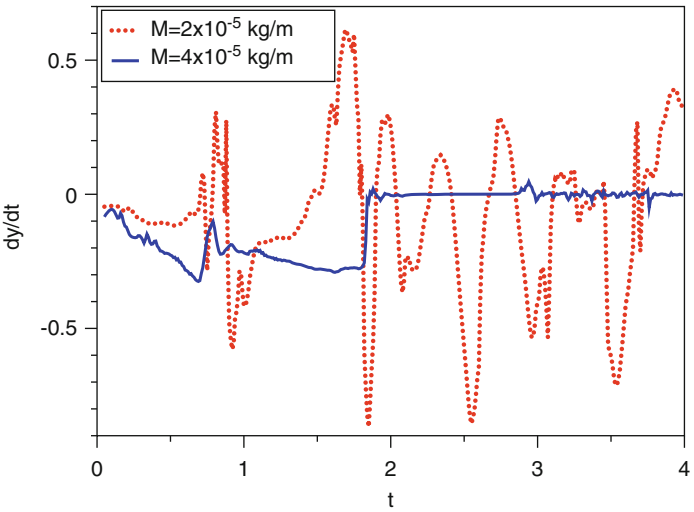

Fig. 17 Vertical velocity (m/s) of the end of the dragline attached to the spider vs. time (s) for free fall in the cavity flow. Spiders with masses per unit length of $M = 2 \times 10^{-5}$ kg/m and $M = 4 \times 10^{-5}$ kg/m are shown. (**a**) t = 0.3 s. (**b**) t = 0.6 s (before release). (**c**) t = 1.04 s (after release). (**d**) t = 1.2 s

By comparing the dragline dynamics with different background winds, we have found that the details of the air movement are important for determining the amount of time the spider spends in the air and the distances traveled. Not only the strength but also the direction and local dynamics of the wind are critical. However, when a spider initiates the climb to a tiptoe position, what are the important signals available to control the subsequent takeoff? To explore this question, we simulate the spider-dragline tethered in the flow to simulate tiptoeing. We then release the spider to examine the dynamics of takeoff.

3.3 Dynamics of Takeoff

Herein, we identify the mechanical factors of takeoff associated with spider ballooning by simulating the spider-dragline system tethered in the flow and released. Beside the flow field and the dynamics of the dragline, the force acting on the tether is analyzed. Note that the spider mass per unit length is fixed at $M = 2 \times 10^{-5}$ kg/m for the subsequent simulations.

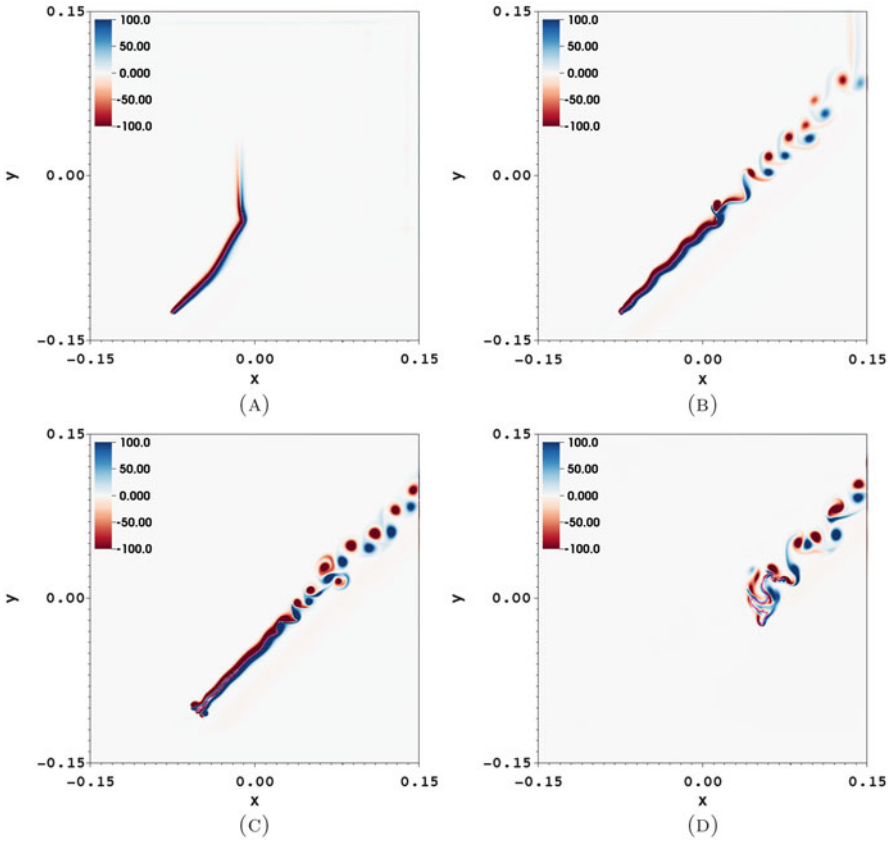

Fig. 18 Vorticity (s^{-1}) snapshots showing the dynamics of a tethered spider-dragline that is released in a 45° wind with strength $|\mathbf{U}| = 1$ m/s. The spider is released at $t = 1$ s. Here, $M = 2 \times 10^{-5}$ kg/m. The *pink curve* is the dragline

3.3.1 Takeoff in Uniform Winds

Four snapshots in time of the vorticity of the flow are shown in Fig. 18. At the earliest time, $t = 0.3$ s (in Fig. 18a), the dragline gradually tilts and aligns with the background wind profile. Subsequently, flapping and shedding of alternately spinning vortices begins as shown in Fig. 18b at t = 0.6 s. Once release occurs (as shown in Fig. 18c-d at t = 1.04–1.2 s), the spider and dragline entangle and move with the background wind. More deformations are created by the vortex in the surrounding air as seen in Fig. 18d at t = 1.2 s.

Figure 19 shows the force per unit length (N/m) acting on the spider when it is tethered ($t < 1$) with different wind directions. The strength of the wind is fixed at $|\mathbf{U}| = 1$ m/s. As the dragline is massless in our model, the comparison confirmed that the tether force is of a similar magnitude. At the beginning of simulation, the

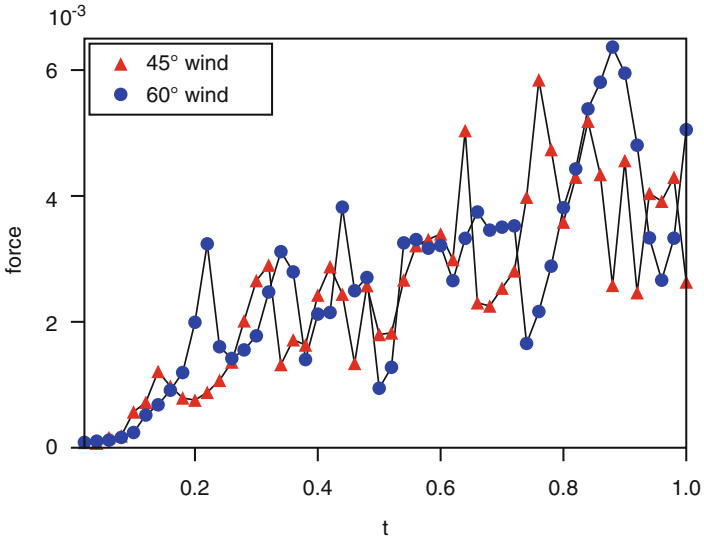

Fig. 19 Force per unit length (N/m) acting on the tether vs. time (s) in a uniform wind moving in two directions (45° and 60°)

forces per unit length increase as the draglines align with the uniform background and are slightly stretched. Around $t = 0.15 - 0.2$ s, vortex shedding begins and the forces per unit length begin to oscillate. This is interesting since laboratory studies show that the length of time spent attempting to takeoff is a factor for whether or not to balloon [35]. This may be correlated to the alignment of the dragline with the wind and the dynamical forces experienced by the spider.

In order to visualize the spider-dragline system in the flow, Fig. 20 shows successive positions of the dragline at selective time points representative of the typical stages of tethering, release, and free flight. The blue line shows the dragline in a uniform wind that is directed 45° from the horizontal, and the red lines show the draglines in a wind directed 60° from the horizontal. The green line shows the initial position for the spider-dragline system. Dashed or dotted lines show the profiles of the dragline while the spider is tethered at position $(-0.75, -0.75)$ and for $t \leq 1$ s. During the tether ($t \leq 1$), the time increment between draglines is $dt = 0.15$ s for both background winds. After the release ($t > 1$ s), the draglines are plotted at $t =$ 2.25, 2.8, 2.9, 3, 3.1, 3.2, and 3.3 s in the 45° wind, and $t = 2.15$, 2.85, 3.05, 3.2, and 3.35 s in the 60° wind. These selective stages demonstrate the dynamics of the spider-dragline but the draglines are not overlapped for visualization purpose.

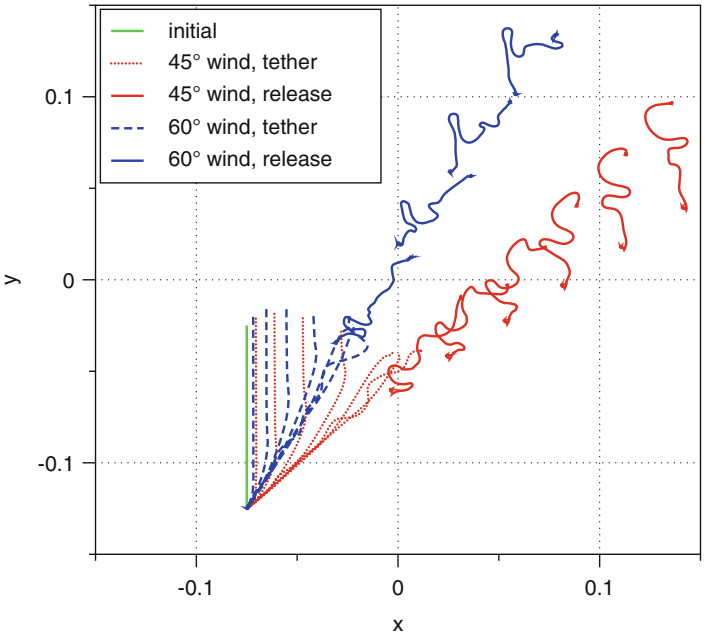

Fig. 20 Snapshots of the dragline at different instances in time for a 45° and a 60° background wind. The spider is released at $t = 1$ s. For both cases, the mass per unit length of the spider is set to $M = 2 \times 10^{-5}$ kg/m. The *green line* is the initial position. During the tether ($t \leq 1$), the time increment between draglines is $dt = 0.15$ s for both background winds. After the release ($t > 1$ s), the draglines are plotted at $t = 2.25$, 2.8, 2.9, 3, 3.1, 3.2, and 3.3 s in the 45° wind, and $t = 2.15$, 2.85, 3.05, 3.2, and 3.35 s in the 60° wind

3.3.2 Takeoff in a Cavity Flow

To further study the dynamics of takeoff, we also simulated the spider-dragline in nonuniform wind, i.e., cavity flow. The setup for cavity flow was the same as performed in Sect. 3.2.2: the flow starts at rest; the horizontal velocity on the top of the domain is set to $U = 3\tanh(100t)$ m/s and the velocities on the other three boundaries are all set to zero; and eddies are formed within the computational domain. For the spider-dragline system, the dragline was initially positioned vertically above the spider. At the beginning of the simulation, the spider was tethered at the center of the domain and was then released in the flow at t = 2 s. The spider mass per unit length in all cases was set to $M = 2 \times 10^{-5}$ kg/m.

Figures 21 and 22 show eight representative snapshots of the vorticity field with the dragline colored in pink. Figure 21 shows four snapshots of the vorticity field during the tether ($t \leq 2$ s). Figure 22 shows four snapshots after release ($t > 2$ s). While the spider-dragline system is tethered, the dragline waves around and interacts with the flow. The dragline sometime breaks up the vortices developed due to the background cavity flow, and the dragline itself sheds vortices in an alternate pattern,

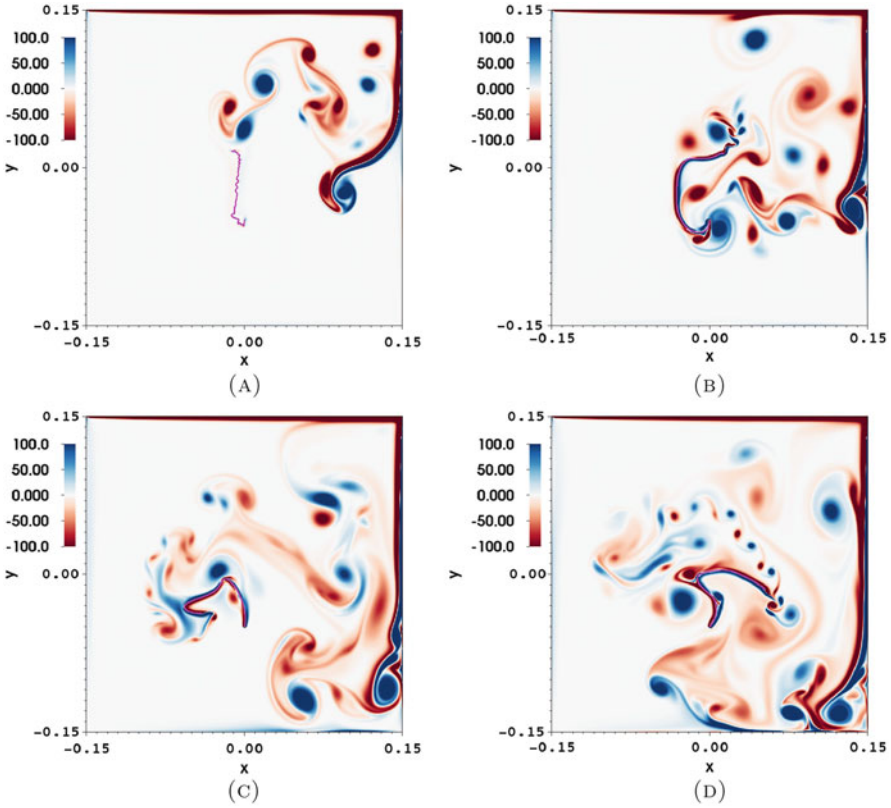

Fig. 21 Vorticity (s^{-1}) snapshots showing the spider-dragline system in the cavity flow. The spider-dragline is tethered for $t \leq 2$ s and released at $t = 2$ s. The dragline is shown in pink. (**a**) t = 0.8 s. (**b**) t = 1.2 s. (**c**) t = 1.6 s. (**d**) t = 2 s

as seen in Fig. 21d. Once the spider-dragline system is released, it free-falls and is advected in the cavity flow, which is dominated by the large eddies moving around the domain.

Figures 23 and 24 show the profiles of dragline during tether and release, respectively. Initially, the dragline is positioned vertically as shown by the green straight line near the center of the domain. From the profiles of the dragline at different instances in time during the tether (Fig. 23), we see that the dragline is swirled by the cavity flow due to the nonzero velocity imposed on the top boundary of the domain. Once the spider-dragline is released from the tether as shown in Fig. 24, it mostly moves with the cavity flow though there are some effects due to gravity. For a longer time simulation, we have observed that the spider continues to be advected round and round the large eddy produced by the cavity flow.

Figure 25 shows the force per unit length acting on tether during $t \leq 2$ s. When $t < 1$ s, the force is negligible. The massive spider is fixed and the massless dragline

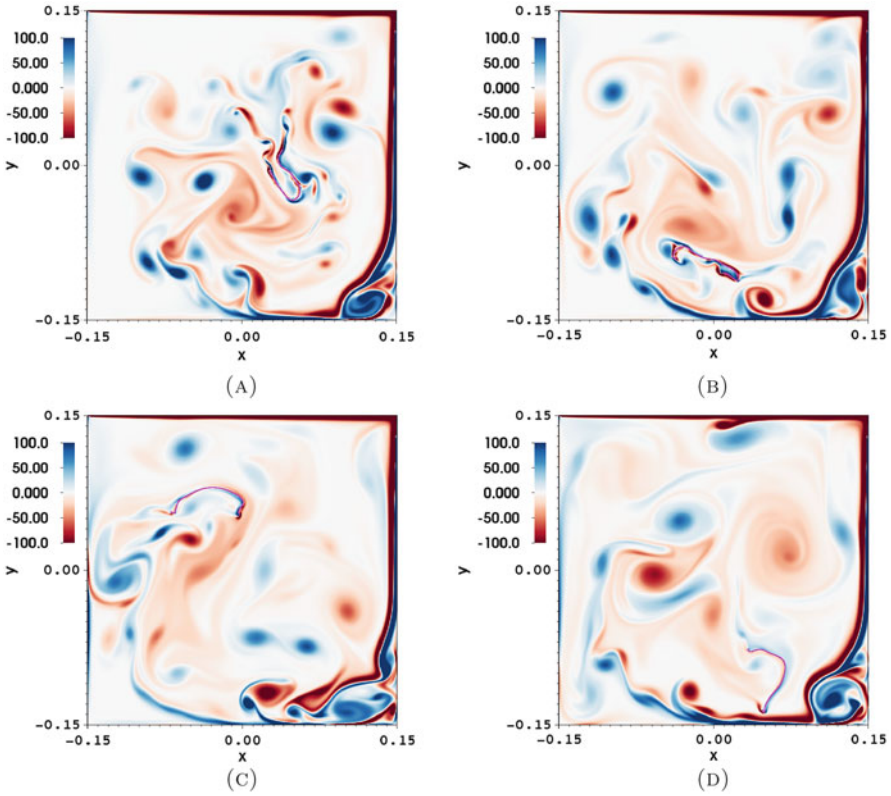

Fig. 22 Vorticity (s^{-1}) at various times in the cavity flow (continued). The spider-dragline is tethered for $t \leq 2\,s$ and released at $t = 2\,s$. (**a**) t = 2.4 s. (**b**) t = 2.8 s. (**c**) t = 3.2 s. (**d**) t = 4 s

does not move in a nearly "quiescent" fluid. The fluid motion produced by the nonzero velocity imposed at the top of the domain generates vortices as shown in Fig. 21a. After $t > 1\,s$, the interaction between the dragline and the flow is intense. Near $t = 1.2\,s$, a vortex with positive vorticity directly reaches the spider. The force is dramatically increased at that time. The instability of the flow field causes large variations in the tether force. When spiders in the tiptoe position can sense this flow force acting on them, they might utilize the force as a signal for further unsteady fluid motion and eventually takeoff given some threshold.

4 Conclusions

By numerically solving the fully coupled fluid–structure interaction problem of a flexible dragline in a viscous fluid, we have revealed new phenomena that cannot be captured by simpler models that neglect how the presence of the dragline affects

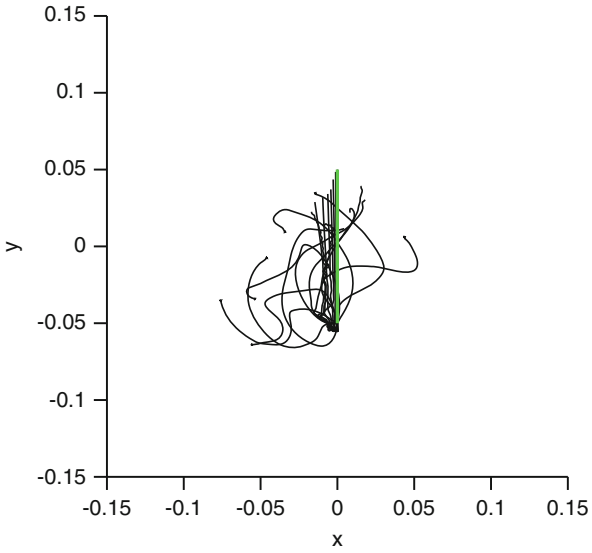

Fig. 23 Temporal snapshots showing the position of the spider-dragline while it is tethered. The spider is tethered for $t \leq 2$ s. The *green line* displays the initial position of the dragline, and the dragline deforms as the cavity flow develops. The time increment is $dt = 0.1$ s between two successive draglines

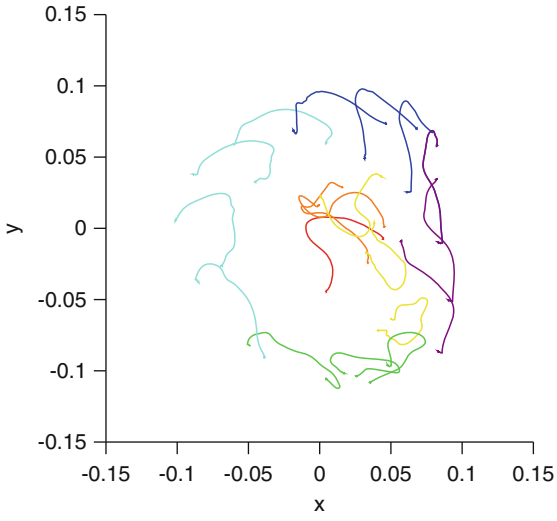

Fig. 24 Temporal snapshots showing the position of the dragline after release ($t > 2$ s). The rainbow colors correspond to advancement in time, with the *black line* showing the position at the end of the simulation. The time increment is $dt = 0.1$ s as Fig. 23

the motion of the air. Our results show that for $Re > 10^3$, strong vortex shedding occurs at the end of the dragline, resulting in oscillations of the dragline itself and some horizontal movement of the spider as it falls through a quiescent fluid. Strong vortex shedding is also present before takeoff, which may generate higher transient

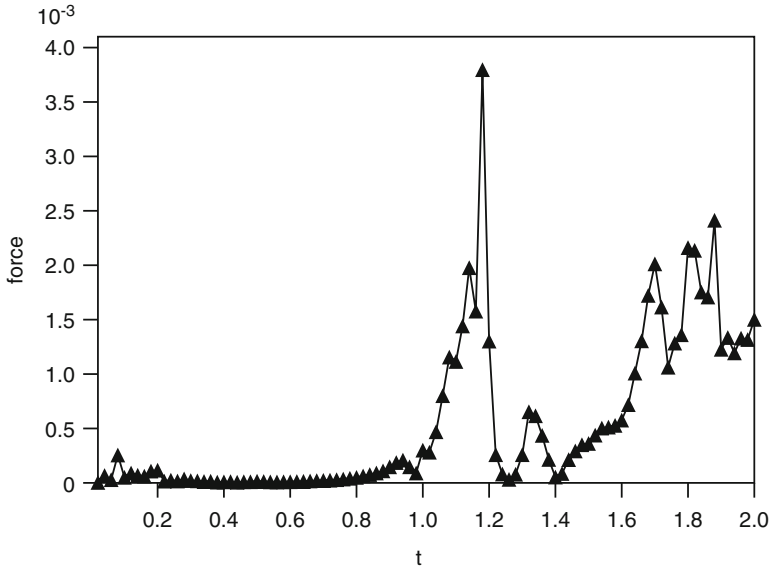

Fig. 25 Force per unit length (N/m) acting on the point where the spider is tethered vs. time (s). The spider is released at $t = 2$ s. The large forces beginning after $t = 1$ s are due to vortices produced by the cavity flow interacting with the dragline

forces to lift the spider into the air. It is also possible that the spiders can sense the vortex shedding frequency and use it to inform whether or not to take off since shedding frequency will vary directly with wind speed. This information could also be used to determine how much longer to make the dragline since the dynamics of the oscillations will also depend upon dragline length.

Our results show that for the parameters considered, the settling velocity varies linearly with the length of the dragline and nonlinearly with the mass of the spider. At the settling velocity, the gravitational force, Mg, balances the drag. Drag varies linearly with length and linearly with velocity for $Re << 1$ and quadratically for $Re >> 1$. For the set of parameters considered, the observed linear relationship suggests a lower Re scaling between force and velocity. When varying the mass of the spider and keeping the length of the dragline constant, a nonlinear relationship is observed between force and velocity since the gravitational force and drag are balanced. This suggests that the larger masses and resulting higher settling velocities push the system to a higher Re scaling.

Direct comparison of settling velocities resulting from the two-dimensional simulations and those of actual three-dimensional spiders is not straightforward. In a two-dimensional simulation, we are essentially modeling an infinitely long sheet which will have higher drag than a one-dimensional line. The mass of the spider must be scaled accordingly, but the relationship between the drag produced by a one-dimensional string and a two-dimensional sheet across intermediate Reynolds

numbers in unsteady flow is not obvious. As a crude estimate, we divide the mass of an actual spider by the diameter of the spider to obtain a mass per unit length. The resulting settling velocities are within the range of those observed for actual spiders [30, 31].

Interestingly, in many simulations, the dragline bends at the tip where the spider is attached. This is perhaps not surprising given the strong vorticity that forms at this leading tip and the low resistance to bending of the dragline. It is not clear if such strong bending would occur in three dimensions or in the presence of electrostatic forces. Similarly, the entire dragline becomes "entangled" in cases where the flow is unsteady. This is particularly true for the movement of the spider within a cavity and also within a crosswind. The tangling of the dragline was also predicted by Reynolds et al. [23]. It is not clear if this phenomenon occurs during actual spider ballooning.

Complex transport dynamics are observed in updrafts and eddies. When eddies are present in the background flow, the dragline may quickly become entangled. It is also possible in these cases for the spider to swirl through the air and remain suspended in the air column as in Fig. 24. In uniform background flows, strong vortex shedding from the tip of the dragline can result in tangling of the dragline after takeoff. Depending upon the entanglement pattern, the dragline may effectively act as a bluff body with finite width, potentially increasing the drag coefficient and lowering the settling velocity.

A natural next step for this work is to move into three dimensions. As mentioned above, the two-dimensional simulations essentially represent a sheet that is infinitely long in the direction moving into and out of the two-dimensional plane. It is likely that the interactions of a sheet with a fluid and its dynamics would be rather different from a one-dimensional dragline. This extension would also allow us to consider multiple draglines that are used by some species of spider for ballooning.

Acknowledgements We are grateful to the National Institute for Mathematical and Biological Synthesis (NIMBioS), which is sponsored by the National Science Foundation (NSF: award DBI-1300426) and The University of Tennessee, Knoxville, for hosting our working group as part of the Research Collaboration Workshop for Women in Mathematical Biology. We especially thank Dr. Anita Layton for organizing the NIMBioS workshop. Additional funding was provided by NSF to KSS (Postdoctoral Research Fellowship 1306883), LAM (CBET 1511427), AC (Graduate Research Fellowship 201315897), and LB (Reeds and Edgerton Funds).

References

1. Batchelor, G.K.: Introduction to Fluid Mechanics. Cambridge University Press, Cambridge (1999)
2. Bell, J.R., Bohan, D.A., Fevre, R.L., Weyman, G.S.: Can simple experimental electronics simulate the dispersal phase of spider ballooners? J. Arachnol. **33**(2), 523–532 (2005)
3. Berger, M.J., Colella, P.: Local adaptive mesh refinement for shock hydrodynamics. J. Comput. Phys. **82**(1), 64–84 (1989)

4. Berger, M.J., Oliger, J.: Adaptive mesh refinement for hyperbolic partial-differential equations. J. Comput. Phys. **53**(3), 484–512 (1984)
5. Bonte, D., Vandenbroecke, N., Lens, L., Maelfait, J.: Low propensity for aerial dispersal in specialist spiders from fragmented landscapes. Proc. R. Soc. B **270**(1524), 1601–7 (2003)
6. Bonte, D., Van Dyck, H., Bullock, J.M., Coulon, A., Delgado, M., Gibbs, M., Lehouck, V., Matthysen, E., Mustin, K., Saastamoinen, M., Schtickzelle, N., Stevens, V.M., Vandewoestijne, S., Baguette, M., Barton, K., Benton, T.G., Chaput-Bardy, A., Clobert, J., Dytham, C., Hovestadt, T., Meier, C.M., Palmer, S.C.F., Turlure, C., Travis, J.M.J.: Costs of dispersal. Biol. Rev. **87**(2), 290–312 (2012)
7. Childs, H., Brugger, E., Whitlock, B., Meredith, J., Ahern, S., Pugmire, D., Biagas, K., et al.: VisIt: an end-user tool for visualizing and analyzing very large data (2012). http://www.osti.gov/scitech/servlets/purl/1170761
8. Coyle, F., Greenstone, M.H., Hultsch, A.-L., Morgan, C.E.: Ballooning mygalomorphs: estimates of the masses of Sphodros and ummidia ballooners. J. Arachnol. **13**, 291–296 (1985)
9. De Meester, N., Bonte, D.: Information use and density-dependent emigration in an agrobiont spider. Behav. Ecol. **21**(5), 992–998 (2010)
10. Glick, P.A.: The distribution of insects, spiders, and mites in the air. Tech. Bull. U.S. Dept. Agric. **673**, 1–150 (1939)
11. Gorham, P.W.: Ballooning spiders: the case for electrostatic flight. ArXiv:1309.4731v1 (2013)
12. Gressitt, J.L.: Biogeography and ecology of land arthropods of Antarctica. In: Mieghem, J., Oye, P. (eds.) Biogeography and Ecology in Antarctica. Monographiae Biologicae, vol. 15, pp. 431–490. Springer, Netherlands/Dordrecht (1965)
13. Griffith, B.: An adaptive and distributed-memory parallel implementation of the immersed boundary (IB) method (IBAMR). https://github.com/IBAMR/IBAMR (2014)
14. Herschlag, G., Miller, L.A.: Reynolds number limits for jet propulsion: a numerical study of simplified jellyfish. J. Theor. Biol. **285**(1), 2369–2381 (2011)
15. Humphrey, J.A.C.: Fluid mechanic constraints on spider ballooning. Oecologia **73**, 469–477 (1987)
16. Kim, Y., Peskin, C.S.: Penalty immersed boundary method for an elastic boundary with mass. Phys. Fluids **19**, 053103 (18 pages) (2007)
17. Miller, L.A., Peskin, C.S.: Flexible clap and fling in tiny insect flight. J. Exp. Biol. **212**, 3076–3090 (2009)
18. Mittal, R., Iaccarino, G.: Immersed boundary methods. Annu. Rev. Fluid Mech. **37**, 239–61 (2005)
19. Nathan, R., Schurr, F.M., Spiegel, O., Steinitz, O., Trakhtenbrot, A., Tsoar, A.: Mechanisms of long-distance seed dispersal. Trends Ecol. Evol. **23**, 638–647 (2008)
20. Peskin, C.S.: Flow patterns around heart valves: a numerical method. J. Comput. Phys. **10**, 252–271 (1972)
21. Peskin, C.S.: The immersed boundary method. Acta Numer. **11**, 479–517 (2002)
22. Reynolds, A.M., Bohan, D.A., Bell, J.R.: Ballooning dispersal in arthropod taxa with convergent behaviours: dynamic properties of ballooning silk in turbulent flows. Biol. Lett. **2**(3), 371–3 (2006)
23. Reynolds, A.M., Bohan, D.A., Bell, J.R.: Ballooning dispersal in arthropod taxa: conditions at take-off. Biol. Lett. **3**(3), 237–40 (2007)
24. Richter, C.J.: Aerial dispersal in relation to habitat in eight wolf spider species. Oecologia **214**, 200–214 (1970)
25. Ronce, O.: How does it feel to be like a rolling stone? ten questions about dispersal evolution. Annu. Rev. Ecol. Evol. Syst. **38**(1), 231–253 (2007)
26. Shao, Z., Hu, X.W., Frische, S., Vollrath, F.: Heterogeneous morphology of Nephila edulis spider silk and its significance for mechanical properties. Polymer **40**(16), 4709–4711 (1999)
27. Sheldon, K.S., Zhao, L., Chuang, A., Panayotova, I.N., Miller, L.A., Bourouiba, L.: Revisiting the physics of spider ballooning. In: Layton, A.T., Miller, L.A. (eds.) Women in Mathematical Biology. Association for Women in Mathematics Series, vol. 8 (2017). doi:10.1007/978-3-319-60304-9_9, 125–139

28. Sobey, I.J.: Oscillatory flows at intermediate Strouhal number in asymmetric channels. J. Fluid Mech. **125**, 359–373 (1982)
29. Stauffer, S.L., Coguill, S.L., Lewis, R.V.: Comparison of physical properties of three silks from Nephila clavipes and Araneus gemmoides. J. Arachnol. **22**(1), 5–11 (1994)
30. Suter, R.B.: Ballooning in spiders: results of wind tunnel experiments. Ethol. Ecol. Evol. **3**(1), 13–25 (1991)
31. Suter, R.B.: Ballooning: data from spiders in freefall indicate the importance of posture. J. Arachnol. **20**, 107–113 (1992)
32. Thomas, C.F.G., Hol, E.H.A., Everts, J.W.: Modelling the diffusion component of dispersal during recovery of a population of linyphiid spiders from exposure to an insecticide. Funct. Ecol. **4**(3), 357–368 (1990)
33. Thomas, C.F.G., Brain, P., Jepson, P.C.: Aerial activity of linyphiid spiders: modelling dispersal distances from meteorology and behaviour. J. Appl. Ecol. **40**(5), 912–927 (2003)
34. Tytell, E.D., Hsu, C.-Y., Fauci, L.J.: The role of mechanical resonance in the neural control of swimming in fishes. Zoology **117**(1), 48–56 (2014)
35. Weyman, G.S.: Laboratory studies of the factors stimulating ballooning behavior by linyphiid spiders (Araneae, Linyphiidae). J. Arachnol. **23**(25), 75–84 (1995)